Electronic Supplementary Information

Flat band potential determination: avoiding the pitfalls

Anna Hankin,[*a,c] Franky E. Bedoya-Lora,[a] John C. Alexander,[b±] Anna Regoutz [b] and Geoff H. Kelsall [a]

Departments of Chemical Engineering [a] and Materials[b], Imperial College London, London, SW7 2AZ.

[c] Institute of Molecular Science and Engineering, Imperial College London

Contents

1. Solution to the Poisson equation for an *n*-type semiconductor and its application to the semiconductor | electrolyte interface

In the absence of interference of surface states, the Mott-Schottky plot will contain contributions from both the semiconductor capacitance and the Helmholtz layer capacitance. The semiconductor capacitance will vary with the degree of band bending while the capacitance of the Helmholtz layer is expected to remain constant. The semiconductor capacitance may be estimated by solving Poisson's equation[1]:

$$\frac{d^2\left(\Delta\phi_{\mathrm{SC}}(x)\right)}{dx^2} = -\frac{\rho(x)}{\varepsilon_0\varepsilon_r} \tag{1}$$

where $\Delta\phi_{SC}$ is negative for $U > U_{FB}$ and positive for $U < U_{FB}$, x is the distance across the depletion region (from surface to the bulk) and ρ is the charge density, which is computed from the Boltzmann distribution:

$$\rho(x) = e(N_D - N_A - n(x) + p(x)) \tag{2}$$

where N_D and N_A are the concentrations of donors and acceptors, respectively, and $p(x)$ and $n(x)$ are the concentrations of electrons and holes in the conduction and valence bands, respectively:

$$n(x) = n_0 \exp\left\{\frac{e\Delta\phi_{\mathrm{SC}}(x)}{k_{\mathrm{B}}T}\right\} \tag{3}$$

$$p(x) = p_0 \exp\left\{-\frac{e\Delta\phi_{\mathrm{SC}}(x)}{k_{\mathrm{B}}T}\right\} \tag{4}$$

where n_0 and p_0 are the bulk concentrations of electrons and holes in the conduction and valence bands, respectively. Hence, under depletion, $\Delta\phi_{SC} < 0$, electrons are driven into the bulk of the semiconductor ($n(x) < n_0$) while under accumulation, $\Delta\phi_{SC} > 0$, electrons migrate to the surface of the semiconductor ($n(x) > n_0$). The converse is true for holes.

For a semiconductor doped only with donors, N_D, integration of equation (1) over the space charge layer[1] yields:

$$\frac{d(\Delta\phi_{\mathrm{SC}})}{dx} = \left[\frac{2e}{\varepsilon_0\varepsilon_r}\right]^{\frac{1}{2}}\left[-N_{\mathrm{D}}\cdot\Delta\phi_{\mathrm{SC}} + \frac{p_0k_{\mathrm{B}}T}{e}\left(\exp\left\{-\frac{e\Delta\phi_{\mathrm{SC}}}{k_{\mathrm{B}}T}\right\} - 1\right) + \frac{n_0k_{\mathrm{B}}T}{e}\left(\exp\left\{\frac{e\Delta\phi_{\mathrm{SC}}}{k_{\mathrm{B}}T}\right\} - 1\right)\right]^{\frac{1}{2}} \tag{5}$$

The differential capacitance of the semiconductor, C_{SC}, is computed according to:

$$C_{\mathrm{SC}} = \frac{dQ_{\mathrm{SC}}}{d(\Delta\phi_{\mathrm{SC}})} \tag{6}$$

where Q_{SC} may be computed using Gauss's law:

$$Q_{\mathrm{SC}} = \varepsilon_0\varepsilon_r\frac{d\Delta\phi_{\mathrm{SC}}}{dx} \tag{7}$$

and hence

$$C_{\mathrm{SC}} = \sqrt{\frac{e\varepsilon_0\varepsilon_r}{2}}\,\frac{-N_{\mathrm{D}} - p_0\exp\left\{-\frac{e\Delta\phi_{\mathrm{SC}}}{k_{\mathrm{B}}T}\right\} + n_0\exp\left\{\frac{e\Delta\phi_{\mathrm{SC}}}{k_{\mathrm{B}}T}\right\}}{\left[-N_{\mathrm{D}}\cdot\Delta\phi_{\mathrm{SC}} + \frac{p_0k_{\mathrm{B}}T}{e}\left(\exp\left\{-\frac{e\Delta\phi_{\mathrm{SC}}}{k_{\mathrm{B}}T}\right\} - 1\right) + \frac{n_0k_{\mathrm{B}}T}{e}\left(\exp\left\{\frac{e\Delta\phi_{\mathrm{SC}}}{k_{\mathrm{B}}T}\right\} - 1\right)\right]^{\frac{1}{2}}} \tag{8}$$

The potential drop across the Helmholtz layer as a function of band bending in the semiconductor is computed according to:

$$\Delta\phi_{\mathrm{H}} = \frac{Q_{\mathrm{SC}}}{C_{\mathrm{H}}} \tag{9}$$

For understanding experimental measurements, C_{SC} needs to be estimated as a function of $U_{electrode}$ rather than $\Delta\phi_{SC}$. This can be accomplished using equation (10), in which the potential drops are estimated through the modelling steps above.

$$U_{\mathrm{electrode}}\ /V(\mathrm{SHE}) = U_{FB}(\mathrm{SHE}) + \Delta\phi_{\mathrm{SC}} + \Delta\phi_{\mathrm{H}} \tag{10}$$

2. Derivation of the Gärtner-Butler equation

A model for the photocurrent flowing across a semiconductor | metal interface[2] is also applicable to the semiconductor | liquid junction. The full expression for the total photocurrent, j_{photo}, generated by monochromatic radiation of intensity I_0, accounting for drift current in the depletion layer of width d_{SC} and diffusion current in the bulk of the semiconductor generated over diffusion length L_p is:

$$j_{\mathrm{photo}} = eI_0\left[1 - \frac{\exp(-\alpha \cdot d_{\mathrm{SC}})}{(1 + \alpha L_{\mathrm{p}})}\right] + \frac{ep_0 D_{\mathrm{p}}}{L_{\mathrm{p}}} \tag{11}$$

d_{SC} is a function of band bending in the semiconductor, $\Delta\phi_{SC}$, and the depletion layer width constant, d_{SC}^0 (width when $\phi_{SC} = 1$ V):

$$d_{\mathrm{SC}} = d_{\mathrm{SC}}^0 \cdot \Delta\phi_{\mathrm{SC}}{}^{\frac{1}{2}} \tag{12}$$

$$d_{\mathrm{SC}}^0 = \left[\frac{2\varepsilon_0\varepsilon_{\mathrm{r}}}{eN_{\mathrm{D}}}\right]^{\frac{1}{2}} \tag{13}$$

Other terms in equation (11) represent the charge of the electron e, diffusion coefficient for holes D_p and the equilibrium concentration of holes in the dark p_0. For a wide gap semiconductor, the last term on the right-hand side of equation (11) is often assumed to make a negligible contribution[3] as p_o is negligible relative to n_o. Therefore, the equation for j_{photo} simplifies to:

$$j_{\mathrm{photo}} = eI_0\left[1 - \frac{\exp(-\alpha \cdot d_{\mathrm{SC}})}{(1 + \alpha L_{\mathrm{p}})}\right] \tag{14}$$

A further simplifying assumption is that the diffusion length L_p is much smaller than the absorption depth α and hence $\alpha L_p \ll 1$, resulting in:

$$j_{\mathrm{photo}} = eI_0[1 - \exp(-\alpha \cdot d_{\mathrm{SC}})] \tag{15}$$

The final assumption is that the depletion width is much smaller than the absorption depth and hence $\alpha \cdot d_{SC} \ll 1$. This enables the Taylor expansion of $\exp(-\alpha \cdot d_{SC})$. Therefore, the underlying assumption of the Gärtner-Butler formulation in equation (16) is that the photocurrent is generated in the depletion region alone.

$$j_{\mathrm{photo}} = eI_0[1 - (1 - \alpha \cdot d_{\mathrm{SC}})] = e\alpha I_0 d_{\mathrm{SC}} = \alpha I_0\left(\frac{2e\varepsilon_0\varepsilon_{\mathrm{r}}}{N_{\mathrm{D}}}\right)^{\frac{1}{2}}(\Delta\phi_{\mathrm{SC}})^{\frac{1}{2}} \tag{16}$$

A plot of j_{ph}^2 against $\Delta\phi_{SC}$ should cross the x-axis at the flat band potential. It should be noted that this relation is only appropriate for the photocurrent alone rather than the total current. The photocurrent can be obtained by subtracting the dark current from the total current measured under illumination. Alternatively, the photocurrent may be separated from the dark current directly by using a lock-in amplifier synchronized to a chopped light source to remove the dark current. However, due to the transient current that occurs when the illumination changes from light to dark and vice versa, there is considerable error in the magnitude of the measured current.

The eError associated with the unverified assumption that $U - U_{FB} \approx \Delta\phi_{SC}$, when interpreting experimental data using equation (16), was discussed in the main manuscript. The determination of $\Delta\phi_{SC}$ as a function of $U - U_{FB}$ can be accomplished using the model described in Section 1 above. Further necessary corrections required by equation (16) have also been described previously[4] and include: (i) use of the spectrally resolved $\sum_\lambda(\alpha_\lambda I_{0,\lambda})$ product to enable prediction of photocurrent under white light, rather monochromatic light, illumination; (ii) account for potential-dependent effects of electron–hole recombination rates, decreasing quantum yields, Φ, and (iii) account for the limitation of the predicted current by the absorbed photon flux that would generate a maximum current density of $I_0 e$. These three corrections result in equation (17).

$$j_{\mathrm{photo}} = \frac{\Phi\left(\frac{2e\left(\sum_\lambda(\alpha_\lambda I_{0,\lambda})\right)^2\varepsilon_0\varepsilon_{\mathrm{r}}}{N_{\mathrm{D}}}\right)^{\frac{1}{2}}(\Delta\phi_{\mathrm{SC}})^{\frac{1}{2}}}{\left[1 + \frac{\Phi\left(\frac{2e\left(\sum_\lambda(\alpha_\lambda I_{0,\lambda})\right)^2\varepsilon_0\varepsilon_{\mathrm{r}}}{N_{\mathrm{D}}}\right)^{\frac{1}{2}}(\Delta\phi_{\mathrm{SC}})^{\frac{1}{2}}}{I_0 e}\right]} \tag{17}$$

3. Choice of equivalent electrical circuits for C_{SC} determination

Circuit 1 (Randles circuit): When a single semicircle is observed on a Nyquist plot generated from EIS data, it is usually modelled using the equivalent circuit shown in Figure S1. C_1 is the interfacial capacitance and can be used with or without correction by the Helmholtz capacitance[5]. The real, Z', and imaginary, $-Z''$, components of impedance generated by this circuit are shown in equations (18) and (19), respectively.

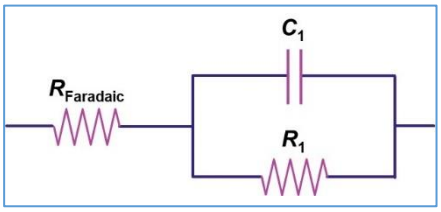

Figure S1. Circuit 1. Randles circuit with one RC loop.

Circuit 1	$Z' = R_{\text{Faradaic}} + \frac{R_1}{(1+\omega^2 R_1^2 C_1^2)}$	(18)
	$-Z'' = \frac{\omega R_1^2 C_1}{(1+\omega^2 R_1^2 C_1^2)}$	(19)

Circuit 2: When two semicircles are observed on a Nyquist plot generated from EIS data, there are multiple equivalent circuit choices. Figure S2 shows a circuit comprising Faradaic resistance and two RC loops, all in series. In previous work, C_1 was assumed to be the semiconductor capacitance and C_2 the Helmholtz capacitance[6]. The real and imaginary components of impedance generated by this circuit are shown in equations (20) and (21), respectively.

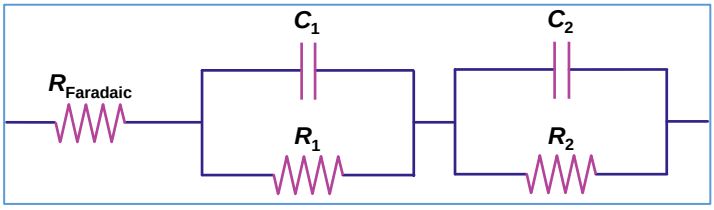

Figure S2. Circuit 2. Two RC loops in series

Circuit 2	$Z' = R_{\text{Faradaic}} + \frac{R_1}{(1+\omega^2 R_1^2 C_1^2)} + \frac{R_2}{(1+\omega^2 R_2^2 C_2^2)}$	(20)
	$-Z'' = \frac{\omega R_1^2 C_1}{(1+\omega^2 R_1^2 C_1^2)} + \frac{\omega R_2^2 C_2}{(1+\omega^2 R_2^2 C_2^2)}$	(21)

Circuit 3: Figure S3 shows a different circuit that would generate two Nyquist semicircles (two time constants), which contains an *RC* loop in parallel with *C*1; this circuit has been used to explain charge trapping by surface states[7] as the second RC loop dominates the impedance at low frequencies. The real and imaginary components of impedance generated by this circuit are shown in equations (22) and (23), respectively.

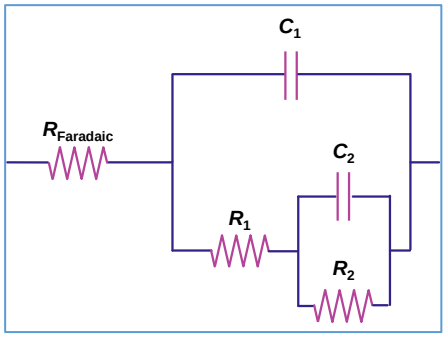

Figure S3. Circuit 3. R_2C_2 loop in parallel with C_1.

Circuit 3	$$Z' = R_{\text{Faradaic}} + \frac{\left[\frac{(R_1+R_2)(1-\omega^2 R_1R_2C_1C_2)}{\omega^2(R_1C_1+R_2C_1+R_2C_2)^2} + \frac{R_1R_2C_2}{(R_1C_1+R_2C_1+R_2C_2)}\right]}{\left[1+\frac{(1-\omega^2R_1R_2C_1C_2)^2}{\omega^2(R_1C_1+R_2C_1+R_2C_2)^2}\right]}$$	(22)
	$$-Z'' = \frac{\left[\frac{R_1R_2C_2(1-\omega^2R_1R_2C_1C_2)}{\omega(R_1C_1+R_2C_1+R_2C_2)^2} - \frac{R_1+R_2}{\omega(R_1C_1+R_2C_1+R_2C_2)}\right]}{\left[1+\frac{(1-\omega^2R_1R_2C_1C_2)^2}{\omega^2(R_1C_1+R_2C_1+R_2C_2)^2}\right]}$$	(23)

Circuit 4: Figure S4 shows a circuit that for many decades has been proposed for describing charge trapping by surface states[8-10]. In this case, the additional resistor and capacitor are in series with each other but collectively in parallel with C_1. The real and imaginary components of impedance generated by this circuit are shown in equations (24) and (25), respectively.

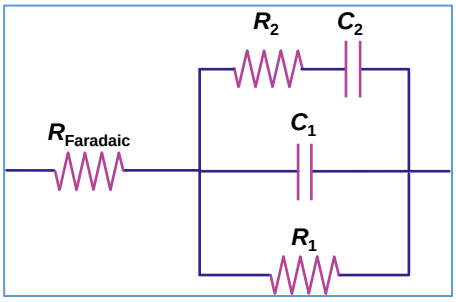

Figure S4. Circuit 4. A second resistor and capacitor in parallel with C_1.

Circuit 4	$$Z' = R_{\text{Faradaic}} + \frac{\omega^2R_1R_2C_2(R_1C_1+R_1C_2+R_2C_2) - R_1(\omega^2R_1R_2C_1C_2-1)}{[\omega^2(R_1C_1+R_1C_2+R_2C_2)^2 + (\omega^2R_1R_2C_1C_2-1)^2]}$$	(24)
	$$-Z'' = \frac{[\omega R_1R_2C_2(\omega^2R_1R_2C_1C_2-1) + \omega R_1(R_1C_1+R_1C_2+R_2C_2)]}{[\omega^2(R_1C_1+R_1C_2+R_2C_2)^2 + (\omega^2R_1R_2C_1C_2-1)^2]}$$	(25)

Circuit simulations: The Nyquist plots generated for equivalent circuits 1, 2, 3 and 4 for identical values of $R_{Faradaic}$, R_1, C_1 and R_2 but varying values of C_2, are compared in Figure S5. Only circuits 2 and 3 can describe the impedance obtained across the α-Fe_2O_3 | 1 M NaOH interface (Figure 8 in the main manuscript), which at all applied potentials exhibited low impedance semicircles at high frequencies and high impedance semicircles at low frequencies.

Circuits 2 and 3 yield identical Nyquist plots when $C_1 << C_2$. However, when C_2 becomes comparable in value to C_1, the extents of overlap between the high and low frequency semicircles differ markedly for the two circuits. Hence, when data can be modelled only using one of these circuits and not the other, the presence of an additional capacitance of similar value to C_{SC} is essentially confirmed.

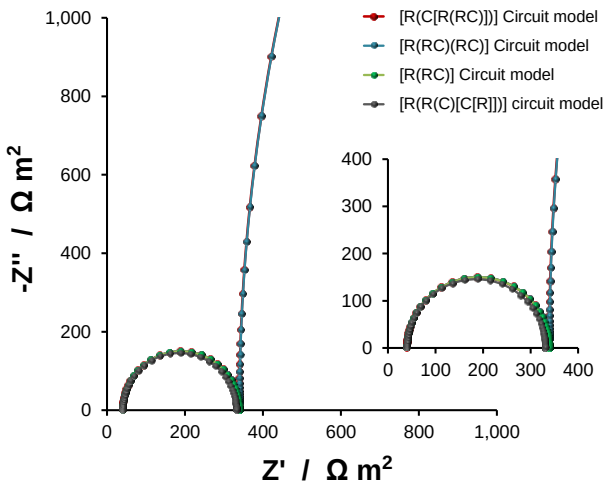

(a) *$R_{Faradaic}$ = 40 Ω m², R_1 = 300 Ω m², C_1 = 10^{-6} F m^{-2}, R_2=10^4 Ω m², C_2 = 10^{-3} F m^{-2}*

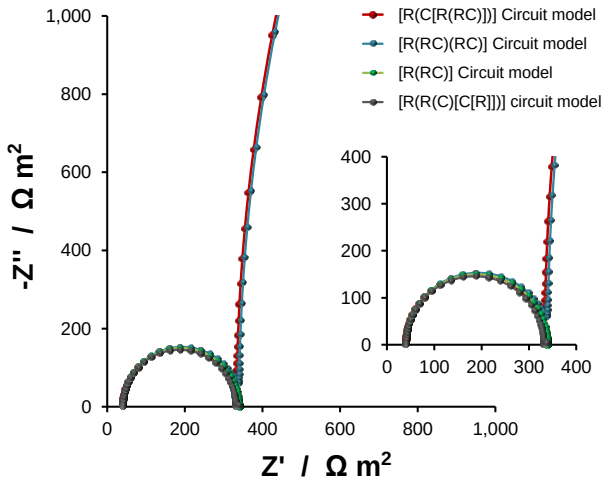

(b) *$R_{Faradaic}$ = 40 Ω m², R_1 = 300 Ω m², C_1 = 10^{-6} F m^{-2}, R_2=10^4 Ω m², C_2 = 10^{-4} F m^{-2}*

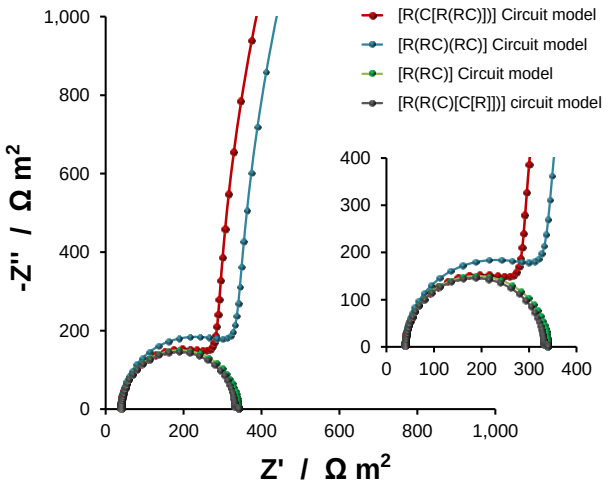

(c) *$R_{Faradaic}$ = 40 Ω m², R_1 = 300 Ω m², C_1 = 10^{-6} F m^{-2}, R_2=10^4 Ω m², C_2 = 10^{-5} F m^{-2}*

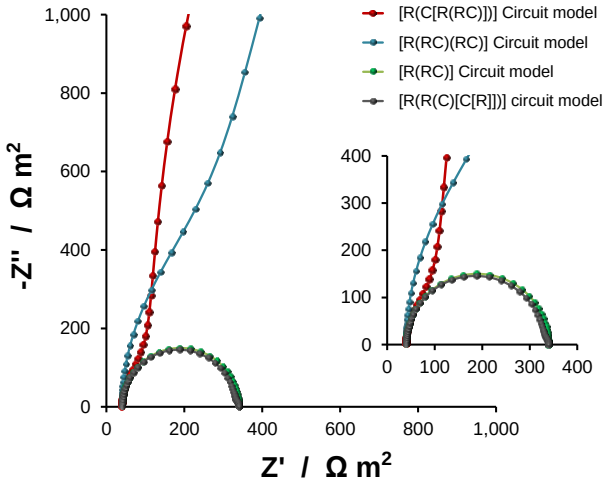

(d) *$R_{Faradaic}$ = 40 Ω m², R_1 = 300 Ω m², C_1 = 10^{-6} F m^{-2}, R_2=10^4 Ω m², C_2 = 10^{-6} F m^{-2}*

Figure S5. Nyquist plots generated for circuits 1, 2, 3 and 4 using $R_{Faradaic}$ = 40 Ω m², R_1 = 300 Ω m², C_1 = 10^{-6} F m^{-2}, R_2=10^4 Ω m² and varying values of C_2. For simplicity, the electrode area was set to 1 m².

4. Conversion of constant phase elements to capacitance

Constant phase elements, CPEs, are used in place of capacitors for fitting equivalent circuits to experimentally determined impedance data, when non-ideal capacitive behaviour is observed, manifested in 'depressed' semicircles in Nyquist plots. The impedance of a constant phase element is given in equation (26). Q_0 has the units of admittance; the exponent n defines the extent of capacitive behaviour: n = 1 for a perfect capacitor and n = 0 for a perfect resistor.

There are two possible approaches for converting CPE to capacitance; both have been applied to interfacial modelling of electrochemical systems:

(i) In the case in which the CPE is modelled to be in parallel with a resistor, the resistance corresponds to the width of the semicircle (along the Z' axis) and its value is used in the conversion[11-13], as shown in equation (27);

(ii) Instead of resistance, the angular frequency at which the maximum in the imaginary component of the semicircle occurs, ω_{max}, can be used as shown in equation (28), where ω_{max} may be determined from plots of complex impedances against the logarithm of the frequency at which they are measured[14].

$$Z(\mathrm{CPE}) = \frac{1}{Q_0(j\omega)^n} \tag{26}$$

$$C = Q_0^{\frac{1}{n}} R^{\frac{(1-n)}{n}} \tag{27}$$

$$C = Q_0(\omega''_{\max})^{n-1} \tag{28}$$

We modelled all our EIS data using the [$R_{Faradaic}(C_1[R_1(R_2C_2)])$] circuit (circuit 3), in which both capacitors needed to be replaced with CPEs to enable a good fit. Equation (28) was not used because ω_{max} could not be reliably determined from plots of Z'' against log(f), as shown in Figure S6(a) for Sample 2. We used equation (27); the quality of the circuit fit to experimental data is shown in Figure S6(b) and extent of capacitances, n, for two loops in Figure S6 (c) and (d). For most applied potentials, n_1, was > 0.8.

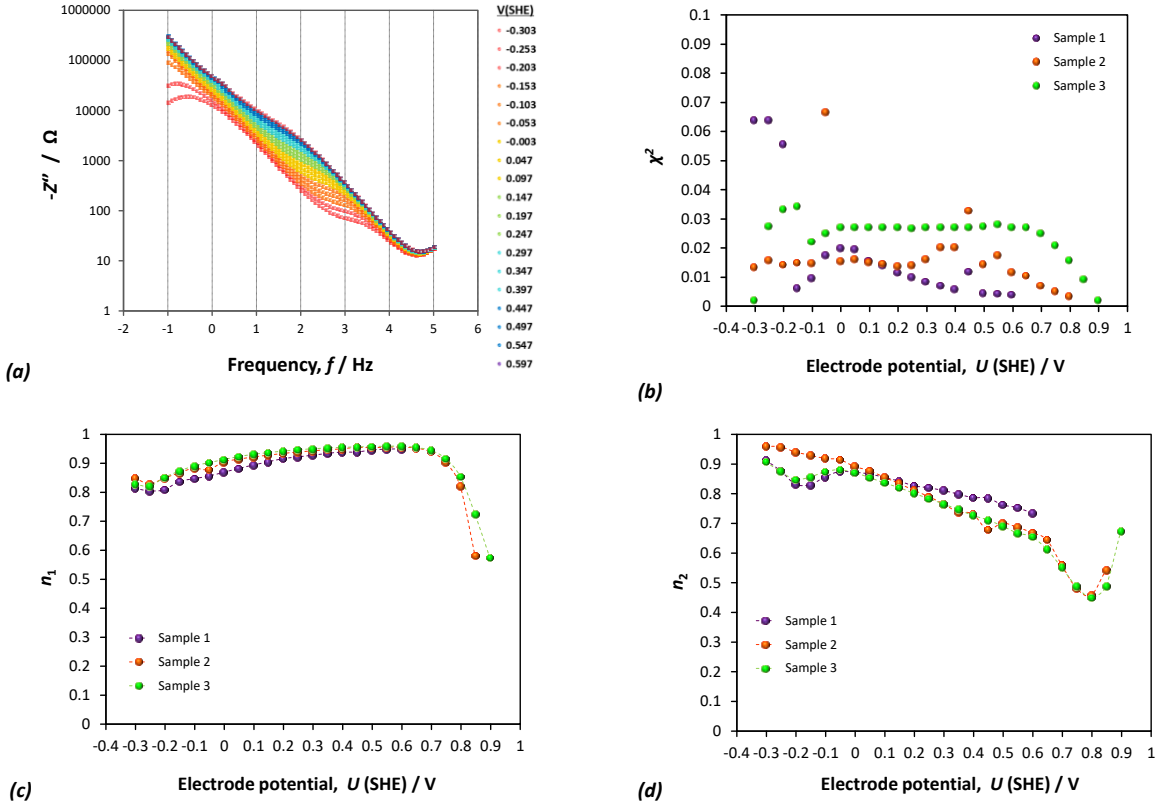

Figure S6. Plot of Z'' against log(f) using raw EIS data collected across the α-Fe_2O_3 (Sample 2) | 1 M NaOH interface; the quality of the [$R_{Faradaic}(CPE_1[R_1(R_2CEP_2)])$] circuit fit to experimental data, χ^2 (b) and numerical information extracted from the fitting: n_1 (c) and n_2 (d).

Since $n_1 < 1$, the use of equation (27) is not strictly accurate, as it does not take into account the additional impedance of the R_2C_2 loop, which is in series with R_1 (see Figure S3). However, equation (27) should yield a sufficiently accurate result, provided $Z'(R_2C_2) << R_1$ at ω_{max}. This can be proven if ω_{max} is known; however, as shown in Figure S6(a), this is not always straightforward. Hence, to verify the accuracy of our *CPE* to *C* conversion, we determined ω_{max} using the distribution of relaxation times, DRT, for EIS data collected at three applied electrode potentials on Sample 2. The DRT method[15-17] is relatively novel and requires complex processing of impedance data. We employed open-access MATLAB-based DRT software 'DRTTOOLS'[15, 18] to determine ω_{max}, and subsequently to compute C_1 using equation (28). Results are presented in Table S1 and confirm that $Z'(R_2C_2) << R_1$ at ω_{max}. The Mott-Schottky plots generated using the two approaches are compared in Figure S7 and show that the capacitance values extracted from CPEs were reliable and cannot be expected to make a significant contribution to the error in flat band determination.

Table S1: *Analysis of EIS data collected on α-Fe_2O_3 Sample 2 in 1 M NaOH using circuit fitting and distribution of relaxation times. [(*)] Capacitance determined using equation* (27)*; [(**)] Capacitance determined using equation* (28)*.*

Applied potential (SHE) / V	$[R_{Faradaic}(CPE_1[R_1(R_2CPE_2))]]$ circuit fitting		DRT fitting	Combined data from both fittings	
	R_1 / Ω	$C_{Interface}^{-2}$ (*) / Ω m²	ω_{max} / rad s^{-1}	$Z'(R_2C_2)$ at ω_{max} / Ω	$C_{Interface}^{-2}$ (**) / Ω m²
-0.253	180	507	8 577	1.00×10^{-2}	544
-0.053	689	634	2 769	3.07×10^{-2}	686
+0.197	2 220	947	1 100	7.08×10^{-13}	993

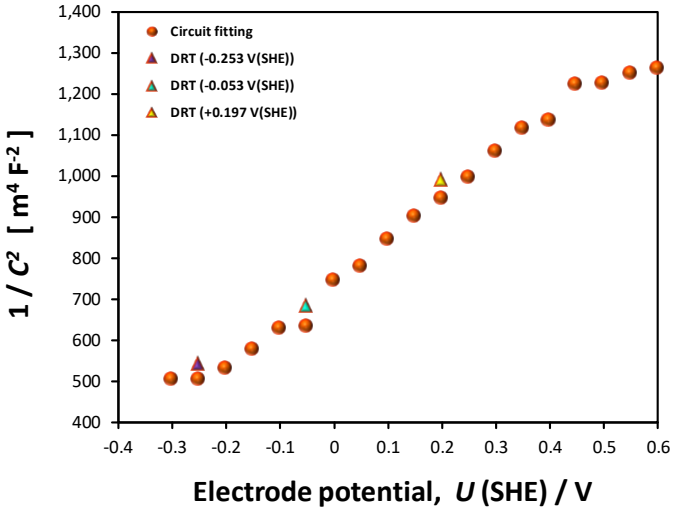

Figure S7. *Mott-Schottky plots based on EIS data collected on α-Fe_2O_3 Sample 2 in 1 M NaOH and processed using circuit fitting (●) and distribution of relaxation times, DRT (▲).*

5. Mott-Schottky analysis of interfacial capacitance, evaluated by electrochemical impedance spectroscopy

EIS measurements were performed on three hematite samples in 1 M NaOH in the dark at potentials in the range -0.3 to +0.8 V (SHE). Each applied potential was perturbed sinusoidally by ±10 mV (p-p) at 75 frequencies in the range 10^{-1} - 10^5 Hz. Prior to the fitting of the $[R_{Faradaic}(CPE_1[R_1(R_2CPE_2)])]$ equivalent circuit to EIS data, the number of data points used for analysis per data set was decreased. Firstly, data collected at applied frequencies higher than 18.6 kHz (10 data points) was removed; these data varied negligibly with applied

potential, as demonstrated in Figure S8, and were believed to be a contribution from the reference electrode. Additionally, data points collected at frequencies below 1.65 Hz (15 data points) were also removed; the additional time constant observed for some potentials at these low frequencies could not be explained and required an unjustifiably complex equivalent circuit. In the end, the [$R_{Faradaic}$(CPE_1[R_1(R_2CPE_2)])] equivalent circuit was fitted to 50 data points per data set, spanning five decades of applied frequencies, which was considered sufficient for accurate determination of 5 circuit elements.

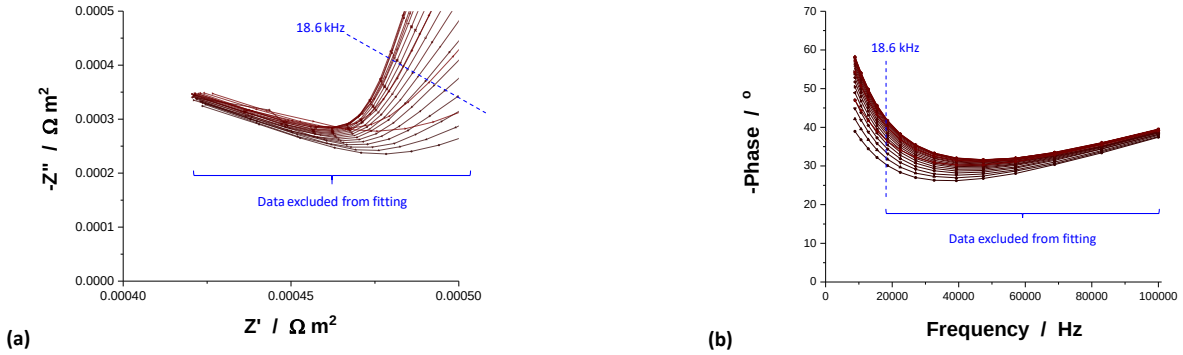

Figure S8. *Features observed in impedance data obtained at perturbation frequencies higher than ≈ 18.6 kHz across the potential range -0.3 V ≤ V (SHE) ≤ +0.9. These features were excluded from analysis by equivalent circuit fitting. The independence of these features from applied potential is demonstrated in (a) Nyquist plot and (b) Bode phase plot.*

Details of the equivalent circuit fitting are shown in Figure S9 for the example of data collected on α-Fe_2O_3 Sample 2 at 0 V (SHE); these data were qualitatively representative of measurements at other potentials.

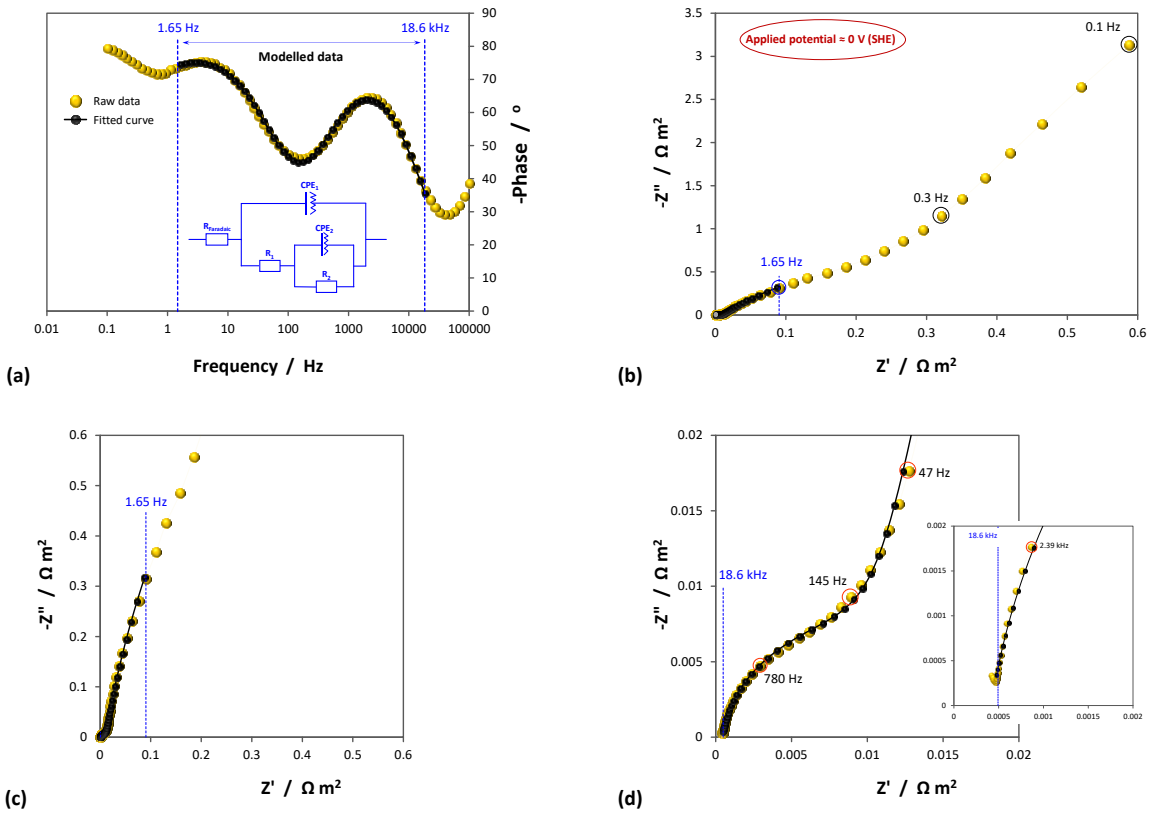

Figure S9. *Bode phase plot (a) and Nyquist plots (b – d) of raw (●) and modelled (●—●) EIS data collected on α-Fe_2O_3 Sample 2 at 0 V (SHE). The modelled data show the range of data used for circuit fitting.*

6. Mott-Schottky plots

Mott-Schottky plots of C^{-2} vs. E are shown for three α-Fe_2O_3 samples in 1 M NaOH in Figure S10 and for an FTO sample in 1 M NaOH in Figure S11. Comparison between these figures shows that FTO is unlikely to have influenced the impedance spectra recorded on hematite and hence was not responsible for the spread in determined flat band potentials.

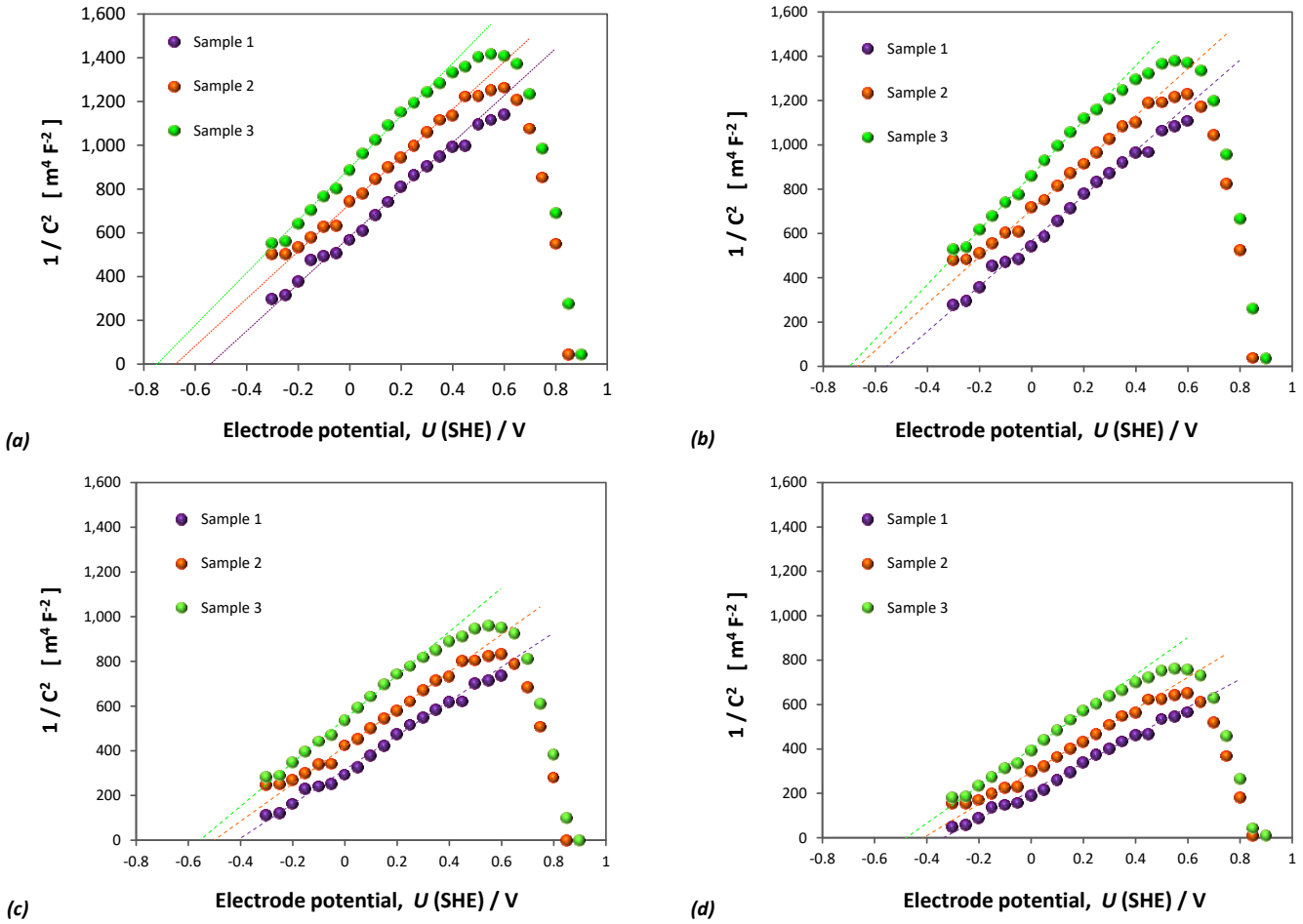

Figure S10. *Mott-Schottky plots from interfacial capacitance of α-Fe_2O_3 in 1 M NaOH: (a) uncorrected for C_H and corrected for C_H = (b) 0.20 F m^{-2}, (c) 0.15 F m^{-2}, (d) 0.10 F m^{-2}.*

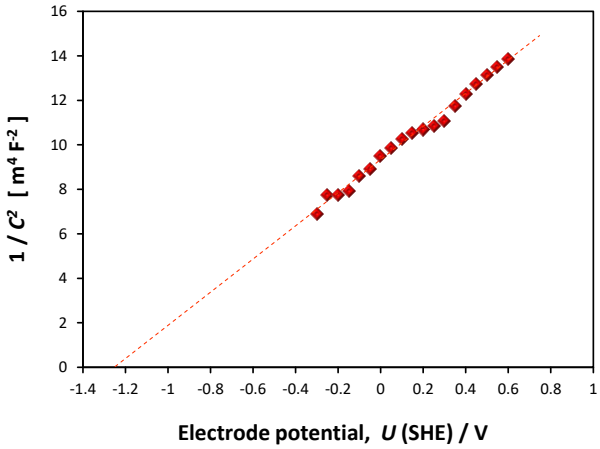

Figure S11. *Mott-Schottky plot from interfacial capacitance of FTO in 1 M NaOH.*

Table S2 lists flat band potentials and charge carrier densities derived from data presented in Figure S10 and Figure S11. Accounting for the range of feasible Helmholtz layer capacitances and assuming that $\varepsilon_r = 80$ for the semiconductor, the range in flat band potentials and charge carrier densities of hematite was -0.77 to -0.32 V (SHE) and 1.47×10^{25} to 2.61×10^{25} m^{-3}, respectively. Based on these data and their wide dispersion, it is unreasonable to suggest a specific flat band potential value.

Table S2: *Flat band potentials and charge carrier densities determined for α-Fe_2O_3 and FTO in 1 M NaOH using Mott-Schottky analysis ($\varepsilon_r = 80$ assumed).*

		Uncorrected	C_H = 0.20 F m^{-2}	C_H = 0.15 F m^{-2}	C_H = 0.10 F m^{-2}
Fe_2O_3 (Sample 1)	**Flat band potential (SHE) / V**	-0.59	-0.44	-0.40	-0.32
	Donor density / m^{-3}	1.64×10^{25}	2.01×10^{25}	2.18×10^{25}	2.61×10^{25}
Fe_2O_3 (Sample 2)	**Flat band potential (SHE) / V**	-0.69	-0.56	-0.52	-0.43
	Donor density / m^{-3}	1.63×10^{25}	1.96×10^{25}	2.10×10^{25}	2.46×10^{25}
Fe_2O_3 (Sample 3)	**Flat band potential (SHE) / V**	-0.77	-0.65	-0.61	-0.52
	Donor density / m^{-3}	1.47×10^{25}	1.80×10^{25}	1.91×10^{25}	2.20×10^{25}
FTO	**Flat band potential (SHE/ V)**	-1.29	-	-	-

Application of the interfacial model to experimentally determined interfacial capacitance data

The interfacial model presented in Section 1 can be used to decrease the spread in the values presented in Table S2. Figure S12 and Table S3 show that the interfacial model was used successfully to narrow the ranges of flat band potentials and dopant densities of our hematite samples in 1 M NaOH to -0.77 to -0.50 V (SHE) and 1.50×10^{25} to 1.70×10^{25} m^{-3}, respectively. Mott-Schottky plots for each sample and different assumed values of C_H (0.1 – 0.2 F m^{-2}) can be modelled using just one charge carrier density. If a different value of ε_r is used in the model, the charge carrier density changes without affecting the flat band potential. The interfacial model enabled the dispersion in flat band potentials to be decreased from 0.45 V to 0.27 V, a significant improvement. However, further increase in confidence is required through other flat band potential determination methods.

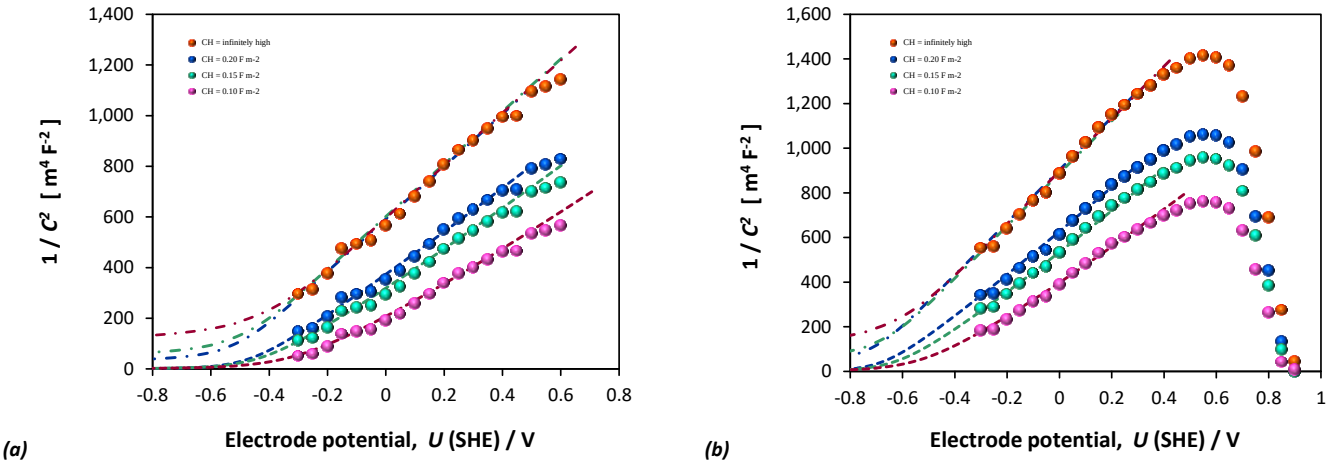

Figure S12. *Experimentally determined (●) and simulated Mott-Schottky plots based on semiconductor (---) and interfacial (- ·- ·-) capacitances for (a) hematite Sample 1 and (b) hematite Sample 2.*

Table S3: *Modelled flat band potentials and charge carrier densities for α-Fe_2O_3 samples ($\varepsilon_r = 80$ assumed).*

		C_H = 0.20 F m^{-2}	C_H = 0.15 F m^{-2}	C_H = 0.10 F m^{-2}
Fe_2O_3 (Sample 1)	**Flat band potential (SHE) / V**	-0.57	-0.56	-0.50
	Donor density / m^{-3}	1.70×10^{25}	1.70×10^{25}	1.70×10^{25}
Fe_2O_3 (Sample 2)	**Flat band potential (SHE) / V**	-0.63	-0.61	-0.57
	Donor density / m^{-3}	1.55×10^{25}	1.55×10^{25}	1.55×10^{25}
Fe_2O_3 (Sample 3)	**Flat band potential (SHE) / V**	-0.77	-0.74	-0.70
	Donor density / m^{-3}	1.50×10^{25}	1.50×10^{25}	1.50×10^{25}

7. Gärtner-Butler analysis of photocurrents

In 1 M NaOH: Net photocurrents measured on hematite and FTO in 1 M NaOH at different scan rates are shown in Figure S13.

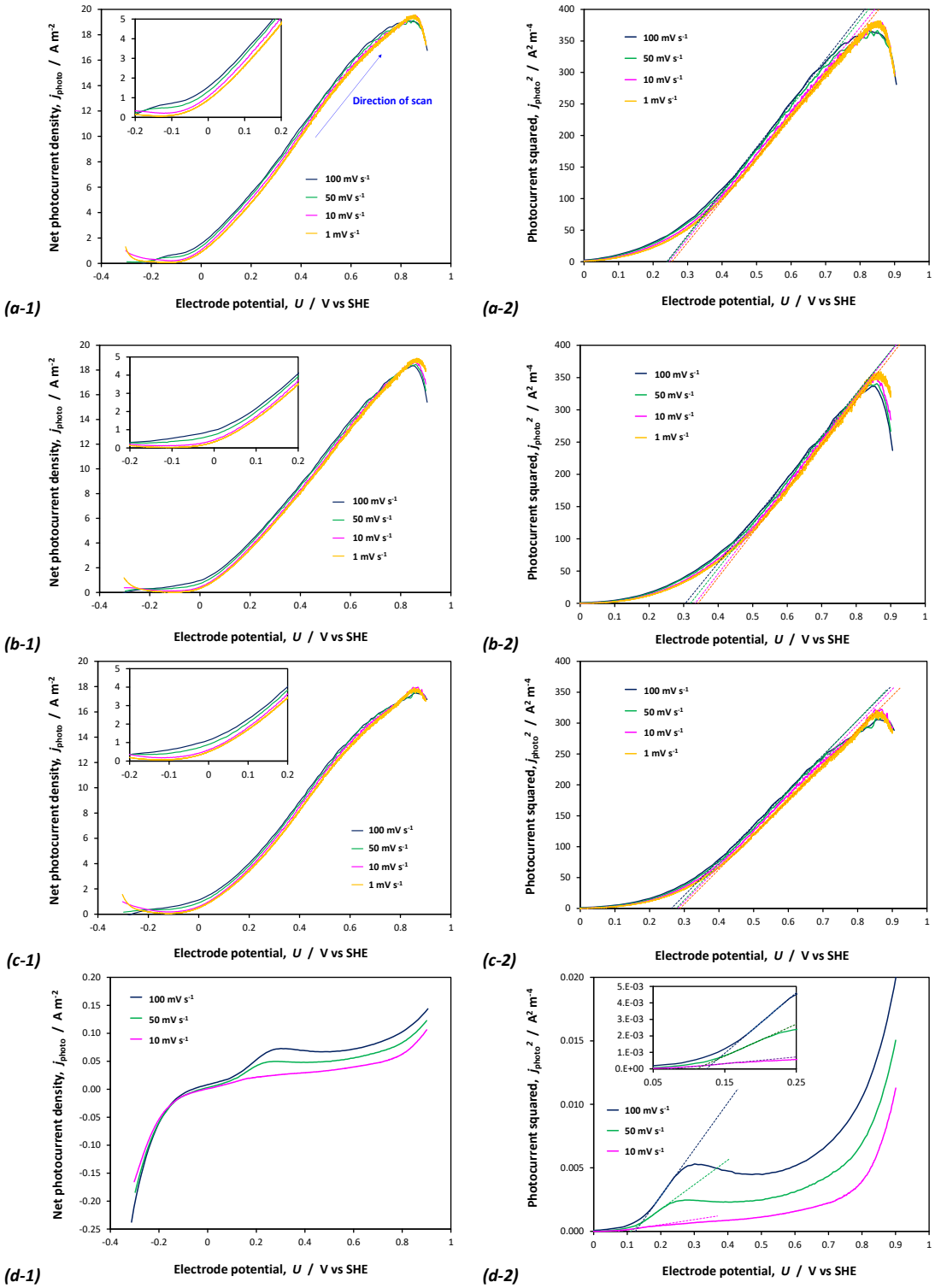

Figure S13. *Effects of electrode potential and scan rate on net photocurrents and their squares for hematite Samples 1 (a-1 & a-2), Sample 2 (b-1 & b-2) and Sample 3 (c-1 & c-2) in 1 M NaOH and FTO in 1 M NaOH (d-1 & d-2). Dashed lines indicate the extrapolation of the linear portions of* j_{photo}^2 *to the x-axis.*

In 1 M NaOH + 0.5 M H_2O_2: Figure S14 shows net photocurrents measured on hematite in 1 M NaOH containing 0.5 M H_2O_2 at different scan rates. No photocurrent could be determined of FTO in this electrolyte at any scan rate.

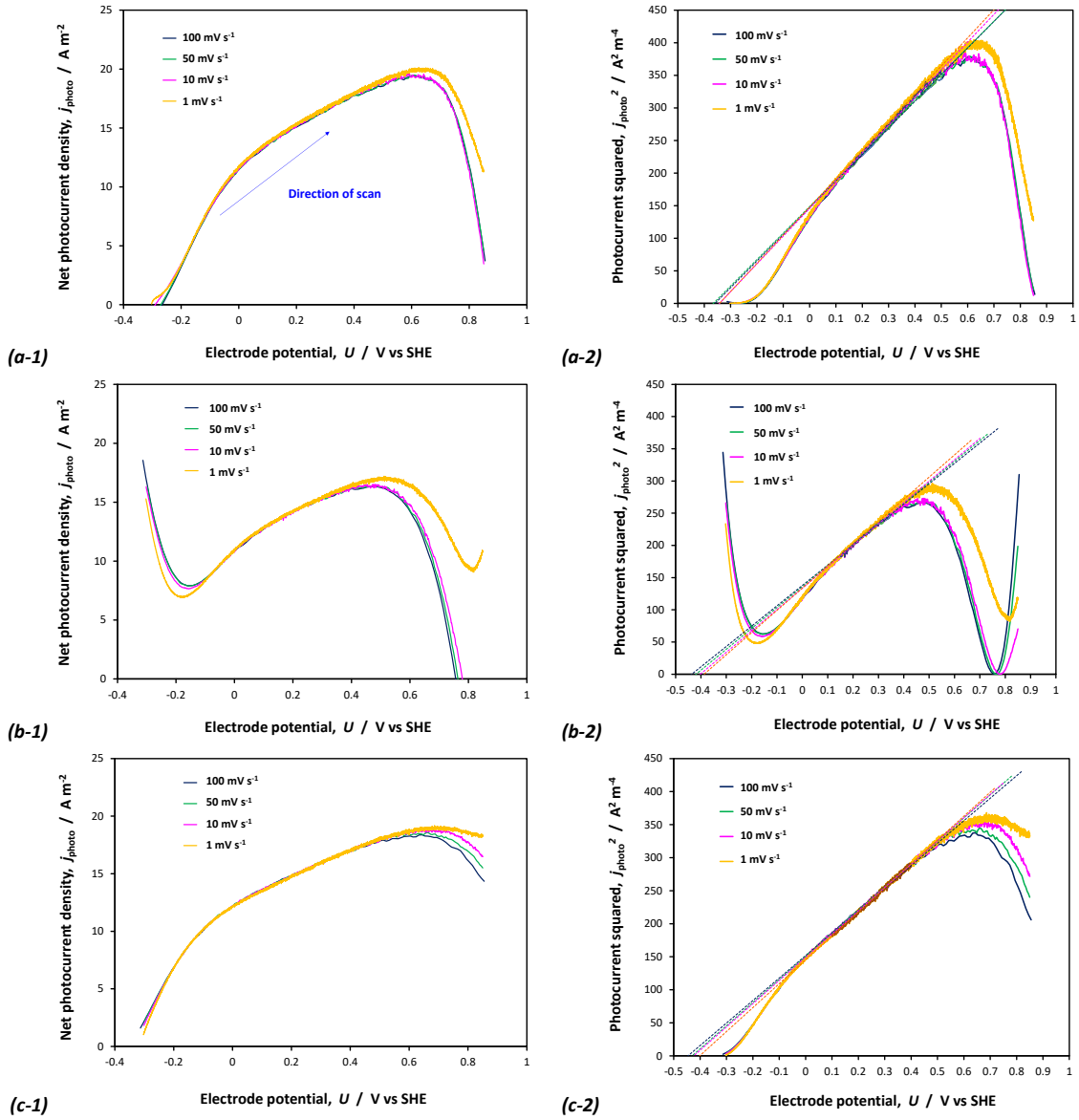

Figure S14. *Effects of applied potential and scan rate on net photocurrents and their squares for hematite samples 1 (a-1 & a-2), 2 (b-1 & b-2) and 3 (c-1 & c-2) in 1 M NaOH. Dashed lines indicate the extrapolation of the linear portions of j_{photo}^2 to the potential axis.*

Summary of flat band potentials determined by Gärtner-Butler analysis

Table S4: *Flat band potentials determined by Gärtner-Butler analysis for α-Fe_2O_3 and FTO samples in 1 M NaOH in absence and presence of 0.5 M H_2O_2*

	Flat band potential (SHE) / V							
	1 M NaOH				1 M NaOH + 0.5 M H_2O_2			
	100 mV s^{-1}	50 mV s^{-1}	10 mV s^{-1}	1 mV s^{-1}	100 mV s^{-1}	50 mV s^{-1}	10 mV s^{-1}	1 mV s^{-1}
Fe_2O_3 (Sample 1)	+0.24	+0.24	+0.25	+0.25	-0.36	-0.37	-0.34	-0.34
Fe_2O_3 (Sample 2)	+0.30	+0.32	+0.33	+0.34	-0.44	-0.42	-0.41	-0.39
Fe_2O_3 (Sample 3)	+0.26	+0.28	+0.28	+0.29	-0.45	-0.43	-0.42	-0.40
FTO	+0.13	+0.11	+0.07	-	-	-	-	-

8. Analysis of chopped photocurrent measurements

Chopped photocurrents on hematite in 1 M NaOH solution

In addition to the previously observed steady state photocurrents at U > -0.1 V (SHE) in 1 M NaOH, the hematite samples exhibited transient photocurrents in the potential region ca. -0.38 ≤ U (SHE) / V≤ -0.15.

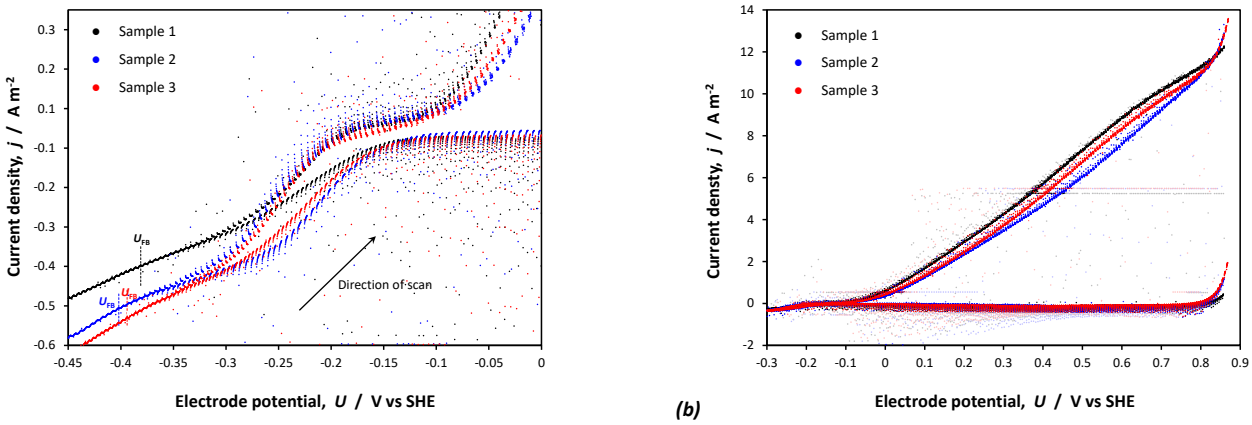

Figure S15. *Effect of potential on chopped photocurrents recorded on three hematite samples in 1 M NaOH at a chopping frequency of 0.3 Hz and scan rate of 1 mV s^{-1}. Two regions where photocurrent was observed are shown in (a) and (b).*

Chopped photocurrents on hematite in 1 M NaOH + 0.5 H_2O_2 solution

As shown in Figure S16, the transient photocurrents observed in 1 M NaOH were not observed in the presence of the H_2O_2 hole scavenger.

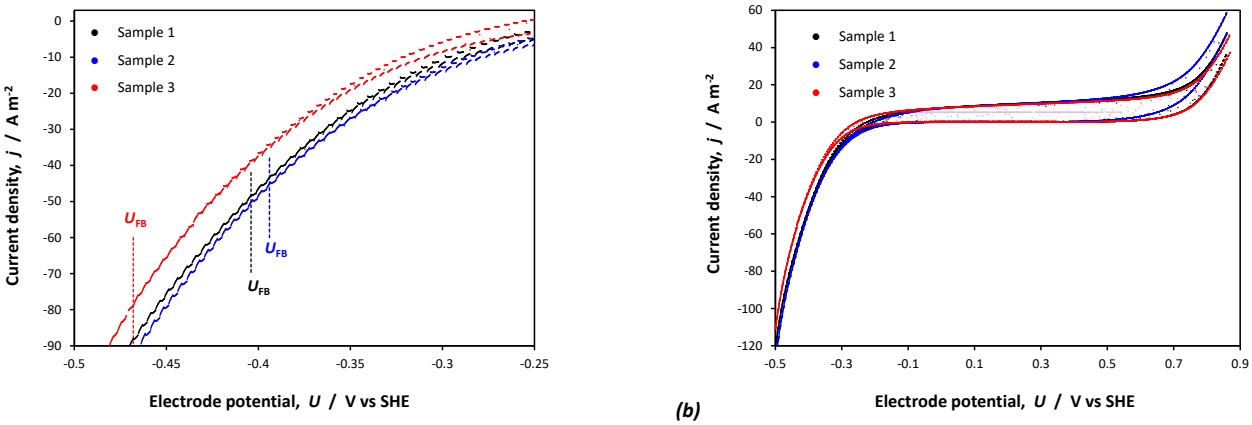

Figure S16. *Effect of potential on chopped photocurrents recorded on three hematite samples in 1 M NaOH + 0.5 M H_2O_2 at a chopping frequency of 0.3 Hz and scan rate of 1 mV s^{-1}.*

Chopped photocurrent on FTO in 1 M NaOH solution

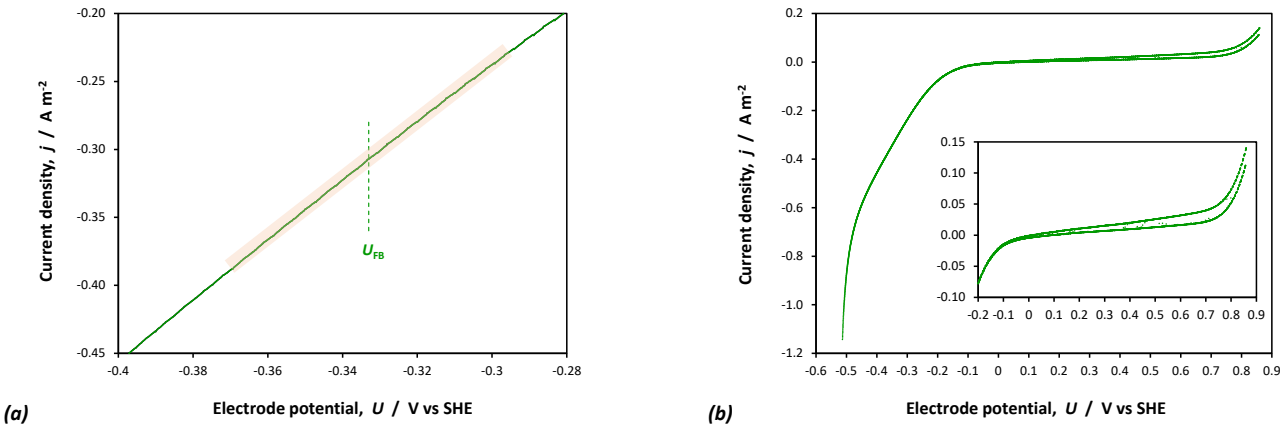

Figure S17. *Effect of potential on chopped photocurrent recorded on FTO in 1 M NaOH at a chopping frequency of 0.3 Hz and scan rate of 1 mV s^{-1}. The shaded region in plot (a) shows the uncertainty in the potential at which photocurrent switched from being negative relative to dark current to being positive relative to dark current.*

Chopped photocurrent on FTO in 1 M NaOH + 0.5 M H_2O_2 solution

In these conditions, the photocurrent on FTO was barely distinguishable from dark current and the flat band potential could not be determined.

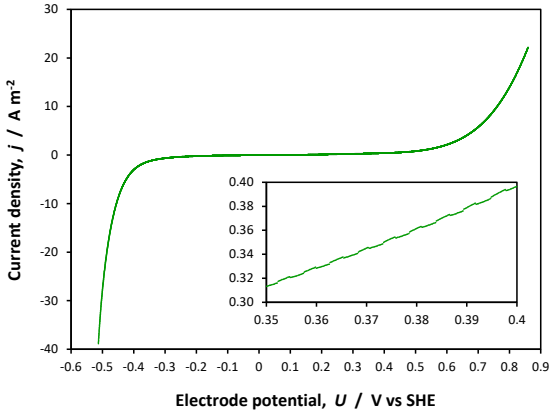

Figure S18. *Chopped photocurrent recorded on FTO in 1 M NaOH + 0.5 H_2O_2 at a chopping frequency of 0.3 Hz and scan rate of 1 mV s^{-1}.*

Summary of flat band potentials determined through chopped photocurrent measurements

The flat band potential values determined on hematite and FTO in the absence and presence of H_2O_2 are reported in Table S5.

Table S5: *Flat band potentials determined from chopped photocurrent voltammetry for α-Fe_2O_3 and FTO samples in 1 M NaOH in absence and presence of 0.5 M H_2O_2*

	Flat band potential (SHE) / V	
	1 M NaOH	**1 M NaOH + 0.5 M H_2O_2**
Fe_2O_3 (Sample 1)	-0.38	-0.40
Fe_2O_3 (Sample 2)	-0.40	-0.39
Fe_2O_3 (Sample 3)	-0.39	-0.47
FTO	-0.33	-

Chopped photocurrents on hematite in 1 M NaOH solution under monochromatic illumination

Chopped photocurrent recorded under monochromatic conditions (λ = 360, 450, 570 and 620 nm) suggested an absence of any bulk inter-band gap states that may have affected the photoelectrode performance, as well as the characteristics of its interface with the electrolyte. Light with energy less than the energy of the band gap ($E_G \approx 2.1$ eV => $\lambda \approx 590$ nm) generated negligible photocurrent.

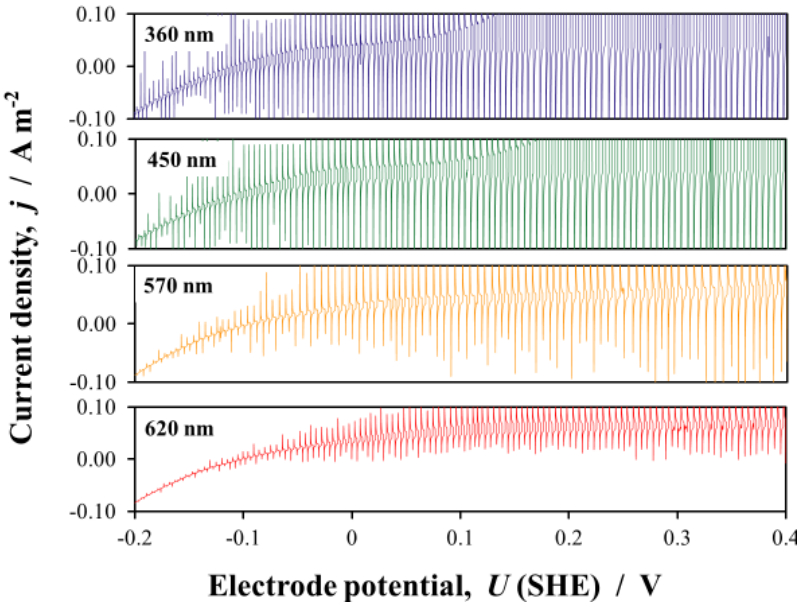

Figure S19. *Chopped photocurrent recorded on hematite in 1 M NaOH, under monochromatic light of different wavelengths; scan rate of 1 mV s^{-1} and chopping frequency of 0.3 Hz were used.*

9. Open circuit potential (OCP) measurements

OCP measurements on hematite and FTO in 1 M NaOH and 1 M NaOH + 0.5 M H_2O_2 solutions

Figure S20 shows the effects of irradiance and electrolyte composition on the OCP recorded on hematite and FTO. Table S6 shows the extracted flat band potentials. Deoxygenation of the electrolyte was found to affect the measured OCP in the dark and under low irradiance, confirming that such measurements require high illumination intensity; the concentration of dissolved oxygen in the electrolyte affects its electrode potential, which in turn affects the Fermi level of the semiconductor upon equilibration, until the illumination is sufficiently strong to control band bending.

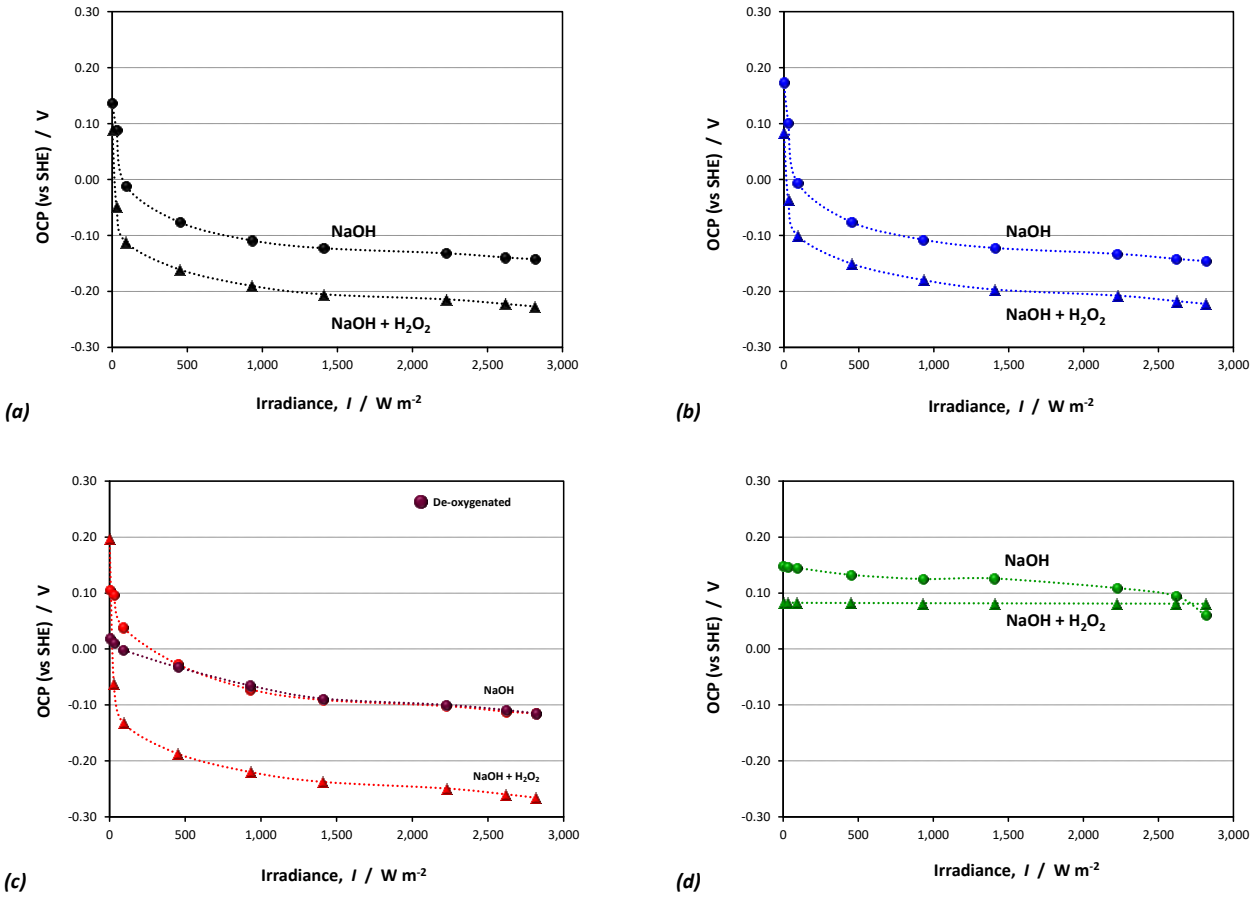

Figure S20. *Effects of irradiance (0 – 2815 W m^{-2}) and electrolyte composition on open circuit potentials of hematite: (a) Sample 1, (b) Sample 2, (c) Samples 3, and FTO: (d). The effect of electrolyte de-oxygenation is shown in (c) for Sample 3.*

Summary of flat band potentials determined through OCP measurements

Table S6: *Flat band potentials determined from open circuit potentials of α-Fe_2O_3 and FTO samples in 1 M NaOH in absence and presence of 0.5 M H_2O_2*

	Flat band potential (SHE) / V		
	1 M NaOH	1 M NaOH (deoxygenated)	1 M NaOH + 0.5 M H_2O_2
Fe_2O_3 (Sample 1)	-0.14		-0.23
Fe_2O_3 (Sample 2)	-0.15		-0.22
Fe_2O_3 (Sample 3)	-0.12	-0.12	-0.27
FTO	+0.06		+0.08

10. Caution against the use of software-automated impedance analysis at single frequencies

The general issues of determining the semiconductor capacitance values from EIS measurements at single frequencies were discussed in the main manuscript. A further issue is discussed below.

In certain software packages, such as Nova (Autolab, Eco-Chemie, The Netherlands), it is possible to record impedance at selected potentials and potential perturbation frequencies specifically for the purpose of automatically obtaining a plot of $1/C^2$ as a function of applied potential, without needing to fit circuits to full EIS data sets collected at each potential. The software automatically fits an *R-C* or an $R_{Faradaic}(RC)$ circuit to the data. In the latter case, the value of $R_{Faradaic}$ is specified by the user and is assumed to be constant at all applied potentials. In this procedure, the circuit is fitted to individual Nyquist plots each comprising one data point only, corresponding to the impedance measured at one potential and at one frequency. The separate capacitance values for each condition are subsequently amalgamated into Mott-Schottky plots.

The accuracy of fitting any circuit to a single data point, depends on the actual capacitance of the interface. Often the capacitance is extracted assuming a *R-C* circuit, rather than the more realistic $R_{Faradaic}(RC)$ circuit. For an *R-C* circuit, the capacitance is evaluated according to equation (29) and for an $R_{Faradaic}$ (*RC*) circuit according to equation (19):

$$-Z'' = j\frac{1}{\omega C} \tag{29}$$

When *Z*″ in equation (29) is compared with Z″ in equation (19), it is clear that they are different. Figure S21 shows the results when *Z*″, computed for an *R*(*RC*) circuit according to equation (19), is then introduced into equation (29) in order to back-calculate the interfacial capacitance using a simpler circuit. It is evident that the capacitance output by equation (29) agrees with the capacitance value input into equation (19) only at high capacitance values and at high frequencies. Hence, the accuracy of using a *R-C* circuit to compute the capacitance of an interface that is characterised by an *R*(*RC*) circuit is highly dependent on the perturbation frequency and on the capacitance of the interface. Hence, often no reliable U_{FB} can be derived, even at high perturbation frequencies.

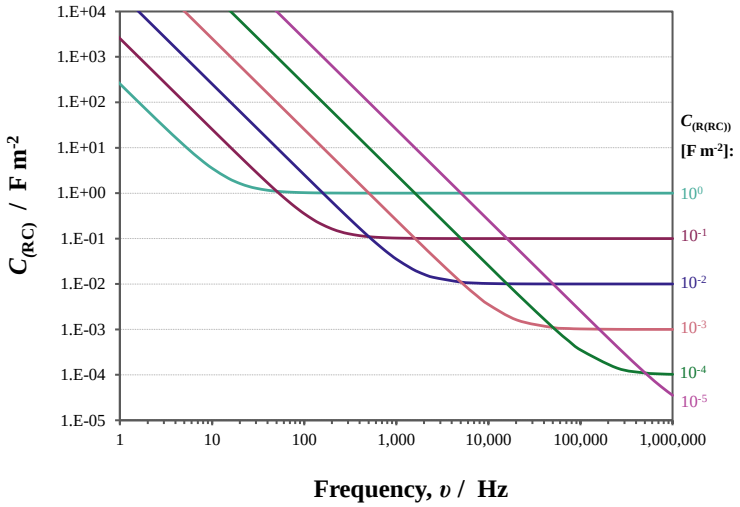

Figure S21. *Effect of perturbation frequency on capacitance computed according to equation* (29) *from Z″, derived using equation* (19) *for* $R_{Faradaic}$ *= 20 Ω,* $R_{Interface}$ *= 1 kΩ and variable* $C_{Interface}$

11. α-Fe_2O_3 characterisation by X-ray photoelectron spectroscopy (XPS)

The surface of the Fe_2O_3 film was characterised using XPS (Thermo Scientific K-Alpha+ X-ray Photoelectron Spectrometer) operating at 2 × 10^{-9} mbar base pressure. This system incorporated a monochromated, microfocused Al Kα X-ray source ($h\nu$ = 1486.6 eV) and a 180° double focusing hemispherical analyser with a 2D detector. The X-ray source was operated at a 6 mA emission current and 12 kV anode bias. Data were collected at 200 eV pass energy for survey and 20 eV pass energy for core level spectra with a 400 µm^2 X-ray beam. A flood gun was used to minimize sample charging. All data were analysed using the Avantage software package. Core levels, shown in Figure S22 (a), were confirmed to be characteristic of Fe_2O_3 and were in excellent agreement with measurements on undoped Fe_2O_3 that was produced by magnetron sputtering specifically for XPS studies.[19] A very small shoulder between ca. 806 and 809 eV, marked with an asterisk, is indicative of a degree of Fe^{2+} polaron presence.[19] The valence band maximum was determined to be 1.54 eV below the Fermi level, from fit to cut-off of valence band feature in XPS, as shown in Figure S22 (b).

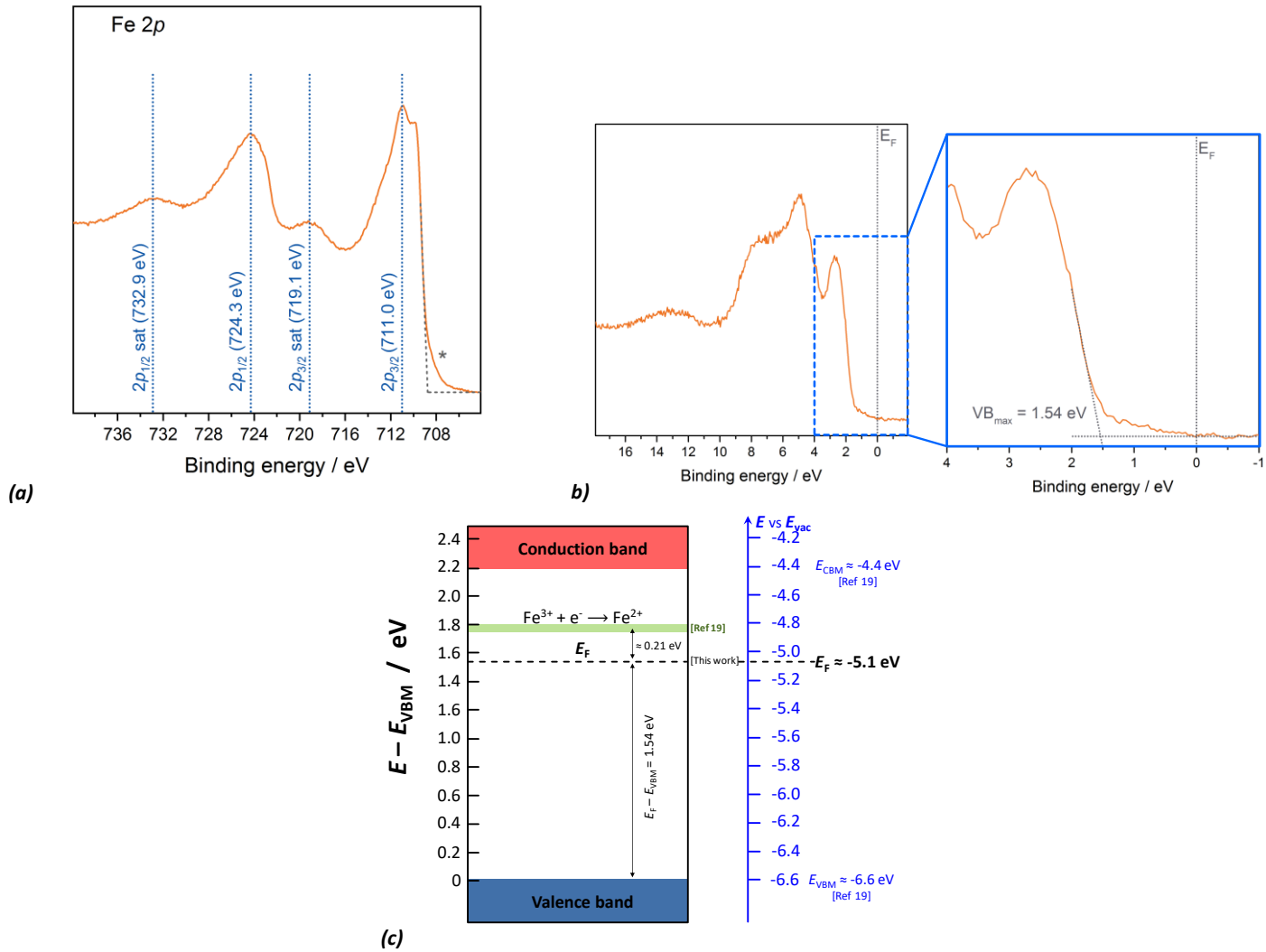

Figure S22. *(a) Fe 2p spectra and (b) valence band maximum energy of α-Fe_2O_3 film on FTO, measured using XPS; (c) the resultant position of the Fermi level relative to band edges and polaron level, arising from Fe^{2+} ions (polaron level was plotted using data from reference 19).*

The purpose of this measurement was to determine the energy separation between the conduction band and Fermi level of our *n*-type Fe_2O_3, which was calculated to be 0.56 eV if the electronic band gap is assumed to be the same as the optical band gap of 2.1 eV. This implies that the conduction band potential of our samples lay 0.56 V negative of the determined flat band potentials. If that were so, hematite would spontaneously evolve hydrogen. Furthermore, if the density of states in the conduction band, N_C, is assumed to be in the range 4.6 × 10^{25} – 1.2 × 10^{26} m^{-3}, as computed previously[20], the separation of 0.56 eV would correspond to a bulk electron density, n_o, in the range 1.6 × 10^{16} – 4.2 × 10^{16} m^{-3}. Such low electron densities are inconsistent with the measurements presented in this study.

However, if the reported electronic band gap of 1.75 eV[19] is assumed, the energy separation between the conduction band and Fermi level may be calculated as 0.21 eV, which is in much better, though not complete, agreement with our experimental observations. It is not conclusive whether the small amount of Fe^{2+} polarons can be responsible for Fermi level pinning and the decrease in the electronic band gap in hematite relative to the optical band gap. The presence of additional capacitance, observed at low frequencies in our EIS spectra, and the Fermi level pinning observed in our OCP measurements, support the hypothesis of the influence of the Fe^{2+} polaron. The MS, GB and CI methods of flat band potential determination support the new electron affinity, shown in Figure S22 (c) as it helps to explain why the flat band potentials we determined were more negative than expected. It is currently unclear how the Fe^{2+} polaron formed on our samples and how the conduction band and the polaron level can affect the various measurements differently. The solution is beyond the scope of this study; hence, more detailed XPS investigations, accompanied by assessment of how electrochemical measurements may impact defect formation, are required in the future to elucidate this.

12. References

1. Pleskov, Y. V.; Ya. Gurevich, Y., *Semiconductor Photoelectrochemistry*. Consultants Bureau: New York, 1986.
2. Gärtner, W. W., Depletion-Layer Photoeffects in Semiconductors. *Physical Review* **1959,** *116* (1), 84-87.
3. Butler, M. A., Photoelectrolysis and physical properties of the semiconducting electrode WO2 *Journal of Applied Physics* **1977,** *48* (5), 1914-1920.
4. Hankin, A.; Bedoya-Lora, F. E.; Ong, C. K.; Alexander, J. C.; Petter, F.; Kelsall, G. H., From millimetres to metres: the critical role of current density distributions in photo-electrochemical reactor design. *Energy & Environmental Science* **2017,** *10* (1), 346-360.
5. Cesar, I.; Sivula, K.; Kay, A.; Zboril, R.; Grätzel, M., Influence of Feature Size, Film Thickness, and Silicon Doping on the Performance of Nanostructured Hematite Photoanodes for Solar Water Splitting. *The Journal of Physical Chemistry C* **2009,** *113* (2), 772-782.
6. Le Formal, F.; Tétreault, N.; Cornuz, M.; Moehl, T.; Grätzel, M.; Sivula, K., Passivating surface states on water splitting hematite photoanodes with alumina overlayers. *Chemical Science* **2011,** *2* (4), 737-743.
7. Klahr, B.; Gimenez, S.; Fabregat-Santiago, F.; Hamann, T.; Bisquert, J., Water Oxidation at Hematite Photoelectrodes: The Role of Surface States. *Journal of the American Chemical Society* **2012,** *134* (9), 4294-4302.
8. Dare-Edwards, M. P.; Goodenough, J. B.; Hamnett, A.; Trevellick, P. R., Electrochemistry and photoelectrochemistry of iron(III) oxide. *Journal of the Chemical Society, Faraday Transactions 1: Physical Chemistry in Condensed Phases* **1983,** *79* (9), 2027-2041.
9. Finklea, H. O., *Semiconductor electrodes*. Amsterdam, New York, Elsevier, 1988.
10. Schefold, J., Impedance and intensity modulated photocurrent spectroscopy as complementary differential methods in photoelectrochemistry. *Journal of Electroanalytical Chemistry* **1992,** *341* (1), 111-136.
11. Harrington, S. P.; Devine, T. M., Analysis of Electrodes Displaying Frequency Dispersion in Mott-Schottky Tests. *Journal of The Electrochemical Society* **2008,** *155* (8), C381-C386.
12. Bedoya, F. E.; Gallego, L. M.; Bermúdez, A.; Castaño, J. G.; Echeverría, F.; Calderón, J. A.; Maya, J. G., New strategy to assess the performance of organic coatings during ultraviolet–condensation weathering tests. *Electrochimica Acta* **2014,** *124*, 119-127.
13. CALDERÓN-GUTIERREZ, J. A.; BEDOYA-LORA, F. E., BARRIER PROPERTY DETERMINATION AND LIFETIME PREDICTION BY ELECTROCHEMICAL IMPEDANCE SPECTROSCOPY OF A HIGH PERFORMANCE ORGANIC COATING. *DYNA* **2014,** *81*, 97-106.
14. Hsu, C. H.; Mansfeld, F., Technical Note: Concerning the Conversion of the Constant Phase Element Parameter Y0 into a Capacitance. *NACE-01090747* **2001,** *57* (09), 2.
15. Wan, T. H.; Saccoccio, M.; Chen, C.; Ciucci, F., Influence of the Discretization Methods on the Distribution of Relaxation Times Deconvolution: Implementing Radial Basis Functions with DRTtools. *Electrochimica Acta* **2015,** *184*, 483-499.
16. Ciucci, F.; Chen, C., Analysis of Electrochemical Impedance Spectroscopy Data Using the Distribution of Relaxation Times: A Bayesian and Hierarchical Bayesian Approach. *Electrochimica Acta* **2015,** *167*, 439-454.
17. Klotz, D.; Schmidt, J. P.; Kromp, A.; Weber, A.; Ivers-Tiffée, E., The Distribution of Relaxation Times as Beneficial Tool for Equivalent Circuit Modeling of Fuel Cells and Batteries. *ECS Transactions* **2012,** *41* (28), 25-33.
18. DRTTOOLS. https://sites.google.com/site/drttools/ (accessed 04/02/2019).
19. Lohaus, C.; Klein, A.; Jaegermann, W., Limitation of Fermi level shifts by polaron defect states in hematite photoelectrodes. *Nature Communications* **2018,** *9* (1), 4309.
20. Hankin, A.; Alexander, J. C.; Kelsall, G. H., Constraints to the flat band potential of hematite photo-electrodes. *Physical Chemistry Chemical Physics* **2014,** *16* (30), 16176-16186.